Physical properties of two-dimensional and quasi-two-dimensional systems

J. D. Hernández Velázquez and A. Gama Goicochea*

Tecnológico Nacional de México, Tecnológico de Estudios Superiores de Ecatepec, División de Ingeniería Química y Bioquímica, 55210 Ecatepec de Morelos, Estado de México, México.
**e-mail: agama@alumni.stanford.edu*

Received 2 August 2024; accepted 13 June 2025

A short review of some recent works on the similarities and differences in the physics of two-dimensional (2D) and quasi-two-dimensional (Q2D) systems by mesoscale models is presented. Three different case studies are reported: (a) two immiscible liquids, (b) a low density, classic Coulomb gas, and (c) dense polymer melts; all of which are under highly confined, Q2D geometry. Among our leading results are the following: the line tension of Q2D systems displays the same scaling exponent as the strictly 2D case. The Q2D Coulomb gas undergoes a topological phase transition closely related to the 2D Kosterlitz-Thouless transition, although important differences arise. Lastly, a scaling law for polymer melts in Q2D is proposed and tested, showing that the structure of the melt goes through fractal transitions with increasing concentration. In addition to the novelty of the results reported here and to their agreement with established theories and experimental data, this work highlights the usefulness of Q2D models to test known and underexplored physical phenomena expected for strictly 2D systems, which are never truly achieved in nature.

Keywords: line tension; topological phase transitions; scaling and criticality; quasi-two-dimensional systems; dissipative particle dynamics.

DOI: https://doi.org/10.31349/RevMexFis.71.061702

1. Introduction

Currently, two-dimensional (2D) materials have acquired relevance in various areas of science and engineering, both because of their technological application and because they raise new challenges to understanding fundamental physical principles. These materials are ubiquitous in branches such as condensed matter [1], biomedicine [2,3], sensing, imaging, and computing technologies [4-6], among others. Although there is nothing in nature that is strictly 2D, there are phenomena observed in experiments using low-dimensional materials that can be understood thanks to theoretical approaches developed for strictly 2D systems. Examples of these developments are studies of critical phenomena [7], topological phase transitions [8], and fractality [9]. However, testing these theories with experiments is not a trivial task. Here is where numerical simulations have proved to be a remarkably useful tool, since systems can be constructed in silico in strictly 2D as well as in Q2D. Some examples can be found in liquid mixtures [10,11], single and binary charged gases [12-15] and polymer solutions [16-18], to name but a few. Despite the evident usefulness of computer simulations to correctly model and predict physical properties of 2D systems, it remains to be fully explored whether there are fundamental differences between the properties of 2D and Q2D systems. No material in nature exists in strictly 2D [19-21], considering that even a single layer of graphene has a thickness of ~ 0.4 nm [22]. However, Q2D materials can be synthesized and tested experimental, as well as in numerical simulations.

In this work, a brief review of three recent case studies of 2D and Q2D systems is presented. Each of these is carried out through coarse-grained simulations using the dissipative particle dynamics (DPD) method [23]. In the first case, a study is presented about a critical phenomenon occurring in Q2D immiscible, binary mixtures of monomeric liquids. The findings of this research show that Widom's hyperscaling relation between the interfacial (2D line) tension (γ) and the correlation length (ξ) [24], is also fulfilled for mixtures having Q2D geometry [25]. In the second case, it is shown that a Q2D, low-density classical Coulomb gas with electrostatic potential $U(r) \sim r^{-1}$, undergoes a topological phase transition that resembles the 2D Kosterlitz-Thouless (KT) transition with electrostatic potential $U(r) \sim \ln(r)$ [8]. Additionally, the influence of an applied magnetic field on structural and dynamic properties of the Q2D charged gas is explored, finding that the structure is unchanged. This is in contrast to what happens with dynamic properties such as the self-diffusion coefficient, which is reduced by the increase of the magnetic field [26]. Lastly, a comprehensive study of Q2D dense polymer melts is presented. A novel fractal scaling law for the osmotic pressure of Q2D polymer melts as a function of the concentration, is proposed and tested. The fractal scaling of the polymer melts in the dense regime is also supported by further analyses made separately for structural properties such as the polymers' contour lengths and their inner monomer-monomer radial distribution functions [27]. These results are directly compared with experimental or simulation data taken from the literature in each of the three cases reviewed here. The outline of this contribution is as follows. Section 2 contains detailed information on the DPD method. Sections 3 and 4 present the information corresponding to the three case studies reported here. Section 5 lists the main general conclusions of the work.

2. Models and methods

The DPD method is a coarse-grained simulation tool, where each bead or DPD particle represents a section of the fluid [23]. The motion of the particles is solved through the discrete integration of Newton's second law, as is done for classical molecular dynamics (MD) [28]. However, the DPD method has a force field that consists of three pairwise forces, which are necessary and sufficient to model simple fluids [29]. They are conservative ($\mathbf{F}_{ij}^{C}$), dissipative ($\mathbf{F}_{ij}^{D}$) and random ($\mathbf{F}_{ij}^{R}$) forces, defined as follows:

$$\mathbf{F}_{ij}^{C} = a_{ij}\left(1-\frac{r_{ij}^{*}}{r_{c}^{*}}\right)\hat{\mathbf{r}}_{ij}, \tag{1}$$

$$\mathbf{F}_{ij}^{D} = -\gamma\left(1-\frac{r_{ij}^{*}}{r_{c}^{*}}\right)^{2}(\mathbf{r}_{ij}\cdot\mathbf{v}_{ij})\hat{\mathbf{r}}_{ij}, \tag{2}$$

$$\mathbf{F}_{ij}^{R} = \sigma\left(1-\frac{r_{ij}^{*}}{r_{c}^{*}}\right)\zeta_{ij}\hat{\mathbf{r}}_{ij} \tag{3}$$

where the three forces have a cutoff radius, r_c^*, such that they vanish when the relative distance between the i-th and j-th particles is greater than or equal to r_c^*, *i.e.*, $r_{ij}^* > r_c^*$. In Eqs. (1)-(3) $\mathbf{r}_{ij}$ and $\hat{\mathbf{r}}_{ij}$ are the relative position vector and its unit vector, respectively; whereas v_{ij} in Eq. (2) is the relative velocity vector and $\zeta_{ij} = \zeta_{ji}$ in Eq. (3) are random numbers with Gaussian statistics [29]. The intensity of each force is determined by the parameters a_{ij}, γ and σ (for $\mathbf{F}_{ij}^{C}$, $\mathbf{F}_{ij}^{D}$ and $\mathbf{F}_{ij}^{R}$, respectively), where σ is interpreted as the noise amplitude, γ as the viscosity coefficient, and a_{ij} is the conservative repulsion between particles.

The a_{ij} parameter in Eq. (1) has a purely repulsive nature and it depends on the chemical composition of the fluid grouped into the beads. Here, the interaction between particles of the same type is defined as [30]:

$$a_{ij} = \frac{k_B T^{*}(N_m\kappa^{-1}-1)}{2\alpha\rho^{*}} \tag{4}$$

where, k_B is Boltzmann's constant, T^* is the temperature of the system, N_m is the so-called coarse-grained degree, κ^{-1} is the isothermal compressibility of the system, α is a numerical constant, and ρ^* is the reduced numerical density of the system. On the other hand, the interaction parameter between particles of different species, a_{ij}, can be estimated through equation [30]:

$$a_{ij} = a_{ii} + 3.27\chi_{ij}, \tag{5}$$

where the Flory-Huggins parameter, χ_{ij}, depends on temperature and can be obtained following the Hildebrand-Scatchard approach [31]:

$$\chi_{ij}(T) = \frac{v_{ij}}{RT}\left(\delta_i(T)-\delta_j(T)\right)^2, \tag{6}$$

where v_{ij} is the partial molar volume, R the gas constant, and δ_i (T) the temperature-dependent solubility parameters of the i-th component. A detailed procedure of this parametrization is reported elsewhere [31].

The thermostat in DPD is built with the parameters of the dissipative and random forces, γ and σ in Eqs. (2) and (3), through the fluctuation-dissipation theorem, given by [29]:

$$\frac{\sigma^2}{2\gamma} = k_B T^{*}, \tag{7}$$

where two of the three parameters are fixed to set up the thermostat. A conventional choice of values is $\gamma = 4.5$ and $\sigma = 3$, which yields internal thermal energy of $k_B T^* = 1$. The latter is referred to as the reduced unit of energy in DPD. The reduced unit of length is the cutoff radius (r_c^*), whose value depends on the coarse-graining degree (N_m) and the reduced number density (ρ), through $r_c = 3.107(\rho N_m)^{1/3}$ Å. Since the length scale in DPD is normalized with the volume of a water molecule ($\sim$ 30 Å^3), the reduced unit of mass in DPD is $m = N_m(3\times 10^{(}-23)$ g). Given these units of mass, length, and energy, the reduced unit of time in DPD is $\tau = \sqrt{(mr_c^2/k_BT)}$. Thus, for a fluid at room temperature with $N_m = \rho^* = 3$, the physical unit of time is $\tau = 3.012\times 10^{(}-12)$ s [32].

To model fluids that involve molecules with more complex architectures, it is necessary to include additional forces that represent the bonding and bending of atomic structures in such molecules, as in surfactants and polymers. In that case, the bonding force that joins two consecutive beads is represented by the Kremer-Grest bead-spring model [33]:

$$F_{ij}^{S} = -k_S(r_{ij}^{*}-r_0^{*})\hat{\mathbf{r}}_{ij}, \tag{8}$$

where k_S and r_0^* are the spring constant and its equilibrium distance, respectively. This harmonic force is frequently used to model complex DPD structures such as surfactants [34,35], lipids [36-38], and polymers [39-41], among others.

The physical confinement of the systems can be modeled by constructing walls made up of particles with frozen locations in two parallel faces of the simulation box, which must be dense enough to prevent fluid particles from penetrating the wall [40,42,43]. There is, however, an alternative approach [25-27,44,45] which consists of adding an effective wall force, acting perpendicularly over all particles near each wall, given by [46]:

$$\mathbf{F}^{W} = a_W\left(1-\frac{z_{iw}^{*}}{z_c^{*}}\right)\hat{\mathbf{z}}_{iw}. \tag{9}$$

This is the approach used in this work. Here, z_c^* is the cutoff distance, z_{iw}^* is the distance to the wall of the i-th particle and the parameter a_w is the maximum repulsion that the wall exerts on the i-th particle. The value of the repulsion parameter is defined as $a_w = (\pi r_c^{*3} a_{ij}\rho_w^*)/12$, where ρ_w^* is the reduced density of the implicit wall [46]. This latter expression for a_w arises from considering a solid wall with hexagonal close-packed crystal structure [47]. Although the parameter a_w emerges from solving exactly the DPD interaction potential, $U^w(z) = a_{ii}r_c^*(1-r_{ij}^*/r_c^*)^2/2$, for $r_{ij}^* < r_c^*$ [47], the force law in Eq. (9) reproduces the results obtained

with the exact force law [46]. Following Gama Goicochea and Alarcón [47] and for densities of $\rho_w^* > 4.4$ and $a_i j = 78$, it is sufficient to model impenetrable walls with the effective force law in Eq. (9) [25-27].

The cutoff distance of the wall force, z_c^*, is chosen as $z_c^* = r_c^*$, in fact, the functional form of such force is modeled in the same fashion as the DPD conservative force [46]. It is chosen so because the force representing the wall is made of DPD particles, whose interaction drops to zero for distances beyond r_c^*. Choosing values of $z_c^* \neq r_c^*$, changes the range of the wall force, which would yield artificial structural changes in the fluid. This aspect is accompanied by alterations in the mechanical properties of the system, since they are related to the internal structure of confined fluids [48]. This type of confinement is computationally more efficient because it avoids the need to perform multiple interactions between fluid particles and the frozen particles in the wall.

The electrostatic interactions between charged particles are modeled using the standard Ewald sums, adapted for the DPD method [28,49,50] using charge distributions instead of point charges. The charge distribution is given by [49,50]:

$$\rho_{ch}(r^*) = \frac{q_i^*}{\pi\lambda^3} e^{-2r^*/\lambda}, \tag{10}$$

where in this Slater-type function, λ is the decay length of the charge. The reduced electrostatic force between the i-th and j-th charge distributions with valences Z_i and Z_j, and separated by a distance r_{ij}^*, is given by [50]:

$$F_{ij}^E = \frac{\Gamma Z_i Z_j}{4\pi r_{ij}^{*2}} \left(1 - \left[1 - 2\beta_E r_{ij}^* (1 + \beta_E r_{ij}^*) \right] \times \exp(-2\beta_E r_{ij}^*) \right), \tag{11}$$

where $\beta_E = r_c^*/\lambda$ and $\Gamma = e^2/k_B T \varepsilon_0 \varepsilon_r r_c^*$; e is the electron charge, ε_0 is the vacuum permittivity, and ε_r is the relative dielectric permittivity of water at room temperature. This force includes the contributions in real space ($\mathbf{F}_{ij}^{E,R}$) and Fourier space ($\mathbf{F}_i^{E,K}$) of the entire range of the Coulomb interaction; further details can be found elsewhere [51]. Although Eq. (11) only works for systems with three-dimensional periodicity, Yeh and Berkowitz [52] showed that the three-dimensional version of the Ewald sums can still be used in confined geometries by adding a force to each charged particle in the confinement direction (for further details, see Refs. [52,53]):

$$F_{i,z} = -\frac{\Gamma q_i^*}{V} M_z \hat{\mathbf{z}}, \tag{12}$$

where M_z is the net dipole moment of the simulation box of volume V.

Different types of external fields can be added to the DPD force field to reproduce stationary flows such as Couette's or Poiseuille's flow [41,54,55]. Another example is the addition of an external magnetic field, as done in one of the case studies presented in this work (see Sec. 3.2). In such case, an external magnetic field is applied perpendicularly to the confinement direction, $B = B_z^* \hat{\mathbf{z}}$. The contribution of $\mathbf{B}$ to each charged particle is calculated with the Lorentz force in its usual form [44]:

$$\mathbf{F}_i^B = q_i^* (\mathbf{v}_i \times \mathbf{B}). \tag{13}$$

3. Simulation details

In this section, the simulation and technical details for the three different quasi-two-dimensional systems studied are provided. To achieve strong confinement in these systems, two parallel walls are placed perpendicularly to the z-direction of the simulation box, modeled by an effective force given by Eq. (9). Periodic boundary conditions are imposed along the x- and y-direction of the simulation box only. In the three different case studies, the coarse-graining degree is fixed at $N_m = 3$; the repulsion parameter of the wall force is chosen as $a_w = 120 k_B T^*/r_c^*$, and the cutoff distance is set at $z_c^* = 1 r_c^*$. All simulations are carried out under canonical ensemble conditions (NVT), namely at constant density and temperature [30]. The integration algorithm is a modified and adapted version of the Velocity-Verlet algorithm for DPD [56].

Finite size effects have been studied in the course of this research, however they do not alter our general conclusions. For the Q2D Coulomb gas, the translational order parameter (TOP) is calculated as a function of temperature, for increasing systems' size along the transversal direction. It is found that the TOP becomes progressively reduced [44], as expected for a KT-type phase transition [8]. For Q2D polymer melts, the fractal properties tend to disappear as the system becomes more three-dimensional; see the Supplementary Information in Ref. [27]. In each case studies reported here, the systems' lateral dimensions are chosen large enough to minimize finite size effects. Lastly, finite size effects have been shown to be minimal in DPD because of the short range nature of its force field [57].

3.1. Two-dimensional and quasi-two-dimensional binary interfaces

In this study, simulations of two immiscible liquids are performed under Q2D geometry and under a strictly 2D setup. The difference between Q2D and 2D systems is that 2D fluids only move on the xy-plane because their degrees of freedom along the z-direction are frozen, while for Q2D fluids the degrees of freedom in the three directions are fully taken into account. In both Q2D and 2D systems, the parameters of the conservative force, a_{ij} [Eq. (1)], between particles of the same species are equal to $a_{ii} = 78.3 k_B T^*/r_c^*$. The cross-interaction parameters are chosen heuristically as $a_{ij} = 100 k_B T/r_c$ and $a_{ij} = 140 k_B T^*/r_c^*$, to produce different immiscibility degrees, therefore they do not represent a specific pair of liquids. For this case study, the size of the simulation box for all systems is $L_x \times L_y \times L_z = 50$

$r_c \times 100\ r_c \times 1 r_c$, yielding $V = 5000 r_c^{*3}$. The total number of particles in all cases is $N = 1.5 \times 10^4$ to maintain a global reduced number density of $\rho^* = 3$. These simulations are run for 50 blocks of 10^4 time steps each, where the first 30 blocks are part of the equilibration phase and the last 20 blocks are used for the production phase, to calculate the averages of properties of interest. The time step is chosen as $\Delta t = 0.01\tau$. The spatial correlation length and the 2D interfacial tension are reported as functions of the increasing temperature, where the internal temperature of the system is defined by the fluctuation-dissipation theorem [Eq. (7)]. In this case study, the particular value of the internal temperature of the system, $k_B T^*$, is chosen under the restriction that $\sigma = 3$ [see Eq. (3)], which immediately defines the constant γ, through Eq. (7).

3.2. Quasi-two-dimensional classical Coulomb gas

Simulations of a low-density classical Coulomb gas are performed to study the effects of the application of an external magnetic field at different temperatures on its structural and dynamic properties. The magnitude of the conservative force parameters (Eq. (1)) for the two components of the Coulomb gas are $a_{ii} = a_{ij} = 78.3\ k_B T^*/r_c^*$; whereas the net charge of all particles is fixed to $|q^*| = 4e$. The parameters used for the Ewald sums (Eqs. (10)-(12)) are chosen as $r_E^* = 3$, r_c^*, $\alpha_0 = 0.969 r_c^{*-1}$, $\lambda = 1.076 r_c^*$, and $\vec{r}^{\max} = (5, 5, 5)$ following Terrón-Mejía *et al*. [49] and Alarcón *et al.* [53]; whereas $\Gamma = 13.87$ and $\beta_E = 0.929$ [50]. The highest magnetic field used for this study was $|B| = B_z^* = 0.1$, in reduced DPD units. The SI conversion factor, considering the typical temperature used in relevant experiments of $T = 1$ K [58,59], is $B \approx 619$ T, which means the magnitude of the highest magnetic field applied is $|B| = 61.9$ T. The Coulomb gas is simulated at reduced density $\rho^* = 0.03$, consisting of $N = 200$ DPD particles, except for systems used to calculate the radial distribution functions, where 3×10^4DPD particles are used. The dimensions of the simulation cell are $L_x = L_y = 80\ r_c^*$ and $L_z = 1\ r_c^*$, yielding $V = 6400\ r_c^{*3}$ for systems with $N = 200$, and $L_x = L_y = 1000 r_c^*$ and $L_z = 1\ r_c^*$, and $V = 10^6\ r_c^{*3}$ for systems with $N = 3 \times 10^4$. The time step chosen for all simulations of both systems is $\Delta t = 0.03\tau$, and they are run for at least $10^7\ \Delta t$ up to $4 \times 10^7 \Delta t$.

For this case study, the translational order parameter and the self-diffusion coefficient of the Q2D charged gas are reported as functions of temperature, *i.e.*, as functions of the coupling constant. Therefore, the internal temperature of the systems, $k_B T^*$, is chosen as an input parameter and it is achieved by fixing $\sigma = 3$ (see Eq. (3)), while the fluctuation-dissipation theorem (Eq. (7)) is used to set the dissipation parameter, γ, defined in Eq. (2), to keep the internal temperature constant at the chosen input value.

3.3. Quasi-two-dimensional polymer melts

A comprehensive study of highly confined polymer melts is carried out to test a proposed scaling law for the osmotic pressure as a function of polymer concentration. The polymers are modeled as linear chains joined by a harmonic potential, as stated in Eq. (8). The spring constant and the equilibrium distance of all bonds are chosen as $k_s = 100 k_B T^*/r_c^{*2}$ and $r_0^* = 0.7 r_c^*$, respectively [54]. There is only one conservative force parameter $a_{ii} = 78.0\ k_B T^*/r_c^*$, since there are only polymer chains. The global density in the system ρ^* is equal to the monomer concentration c^* because there is no solvent, only polymer chains. Different values of the polymerization degree (N) are modeled and the total number of monomers changes with N. For systems where $N = 500$, 600, 800, 1000, 1500, 2000, 3000, and 4000, the total number of monomers is $N_{\text{Tot}} = 1.2 \times 10^4$; and for those where $N = 2500$ and 3500, the total number of monomers is $N_{\text{Tot}} = 1.25 \times 10^4$ and 1.05×10^4, respectively.

The width of the simulation cell in all systems is fixed at $L_z = 1.87 r_c^*$, which is approximately the thickness of two layers of fluid, under standard conditions. On the other hand, the lateral sizes of the simulation box ($L_x = L_y$) are adjusted, depending on the monomer concentration (c^*) of the system, as follows:

$$L_x = L_y = \sqrt{\frac{N_{\text{Tot}}}{c * L_z}}, \tag{14}$$

where c^* varies from $c^* = 2$ up to $c^* = 4$, in increments of 0.1 units. All simulations are run for at least 100 and up to 1000 blocks of $2 \times 10^4 \Delta t$ each. The equilibrium phase consists of the first 50% of the total number of blocks, while the last 50% are used for the production phase. The time step chosen for these simulations is $\Delta t = 0.03\tau$. For this case study, the internal temperature of all systems is fixed at $k_B T^* = 1$, setting the parameter $\sigma = 3$, which yields $\gamma = 4.5$, as established by the fluctuation-dissipation theorem, Eq. (7).

4. Results and discussion

4.1. 2D- and Q2D binary interfaces

The results on 2D and Q2D water-oil interfaces are presented and discussed in what follows. The correlation length (ξ) and the line tension (γ) between them are calculated as functions of temperature and compared with predictions from critical phenomena using scaling laws. From this comparison, the scaling exponents v and μ, corresponding to ξ and γ, respectively, are extracted near the critical temperature T_c. These two properties scale with temperature as [60]

$$\xi(T) = \xi_0 \left(1 - \frac{T}{T_c}\right)^{-v}, \tag{15}$$

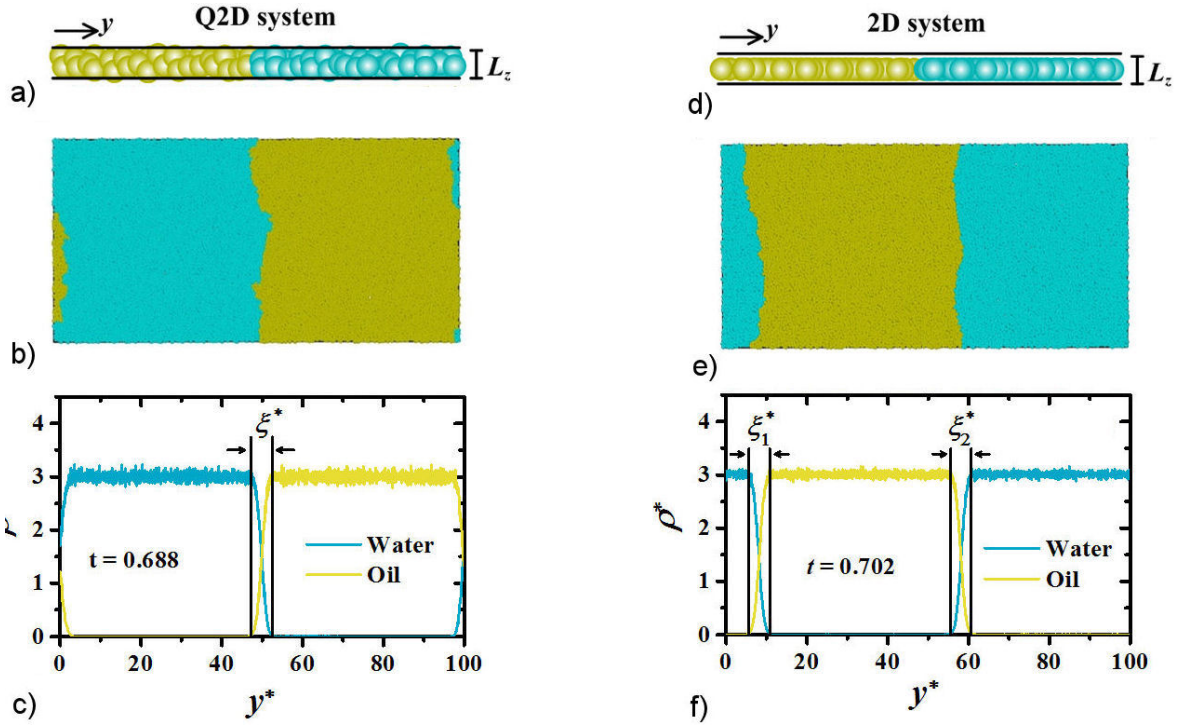

FIGURE 1. a), d) Schematic representation of the quasi-two-dimensional (Q2D) and two-dimensional (2D) geometries of the binary mixtures, with $L_z = 1$. b), e) Snapshots of the Q2D and 2D interfaces generated from the last time step of the simulations, for systems at relatively low reduced temperatures, $t = 0.688$ and $t = 0.702$, respectively. c), f) Number density profiles for Q2D and 2D systems at relatively low reduced temperatures (where $t \equiv 1 - T^*/T_c^*$), showing a well-formed interface. The vertical bars indicate the correlation length (ξ), which is defined as the thickness of the interface; see main text for details. Both axes in c) and f) are in reduced DPD units. Figures adapted from Ref. [25].

and

$$\gamma(T) = \gamma_0 \left(1 - \frac{T}{T_c}\right)^{\mu}, \tag{16}$$

where ξ_0 and γ_0 are the asymptotic values of the correlation length and line tension when $T \to 0$, respectively. As the temperature nears the critical point, the contribution to the interfacial tension of droplets of size $\sim \xi^d$ of one liquid immersed in another is $k_B T/\xi(d-1)$, where d is the Euclidean dimension [61]. Thus, the exponents in Eqs. (15) and (16) are not independent from one another, $\mu = (d-1)\nu$. Testing this relationship for Q2D systems is the main purpose of this case study.

The correlation length of the 2D and Q2D systems is estimated from the thickness of the interfacial region, using the averaged density profiles along the direction perpendicular to the interface [62]. The first derivative of the reduced density as a function of the coordinate y, $d\rho^*\ (y^*)/dy^*$, is calculated to determine the region where the slope of each density function drops zero [25], as indicated by the vertical bars in Figs. 1c) and 1f). The correlation length can be estimated also from the radial distribution functions (RDFs) between water and oil beads, although the calculation employing the density profiles is more precise. That is because the RDFs are typically less sensitive to changes in the external temperature. Appendix A provides detailed information about the methodologies to estimate the spatial correlation length, ξ^*, through the RDF and density profile analyses. Figure 1 shows a schematic illustration of the Q2D and 2D interface models [Figs. 1a) and 1d)], along with a snapshot and a typical density profile of each system [Figs. 1b)-1c) and 1e)-1f), respectively].

The critical temperature of the system is obtained by extrapolating to the temperature when the liquid mixture becomes homogeneous. This procedure works because, as the temperature approaches T_c^*, $\xi^* \to \infty$, so that beyond the critical point the mixture becomes a single, homogeneous fluid. Here, it is found that the critical temperature depends strongly on the conservative force parameters, a_{ij} [see Eq. (1)]. For systems strictly in 2D, the critical temperature is found to be $T_c^* = 2.5$ when the conservative force parameter is chosen as $a_{ij} = 100$, while $T_c^* = 6.6$ when $a_{ij} = 140$. These values are to be compared with those obtained for Q2D systems, with critical temperatures of $T_c^* = 2.4$ and $T_c^* = 6.2$, when $a_{ij} = 100$ and $a_{ij} = 140$, respectively. It should come as no surprise to find that T_c^* is higher for mixtures having a stronger repulsion between the two components, since the nature of the DPD conservative force is purely repulsive, *i.e.*, the lower the value of a_{ij} the less repulsion between the i-th and j-th DPD species. Therefore, a binary mixture with larger a_{ij} will require more thermal energy to achieve the breakdown of the interface and bring the

system to homogeneity. Notice also that there is very little difference between the critical temperature values predicted for strictly 2D systems and for Q2D systems.

The obtain the interfacial tension, the components of the pressure tensor are calculated first, using the virial method [28,63]. Then, the interfacial tension is calculated by integrating the difference between the normal and tangential components of the system's pressure tensor, as follows:

$$\gamma^*(y^*) = \int_0^{L_y} [P_N(y^*) - P_T(y^*)]dy^*, \qquad (17)$$

where $P_N = \langle P_{yy} \rangle$ and $P_T = \langle P_{xx} \rangle$ are the normal and tangential components of the pressure tensor, respectively. The angular brackets refer to quantities averaged over the whole time of the production phase of the simulations. In this case, the interfacial tension is called the line tension because of the low thickness of the interface that renders the fluids 2D or Q2D. Therefore, the z-component of the pressure tensor for Q2D systems is not taken into account in the calculation of γ^*. In the calculation of the components of the pressure tensor, P_{xx} and P_{yy}, only the conservative force (F_{ij}^C) contributes to virial [28], since the F_{ij}^D and F_{ij}^R contributions are zero when the system reaches thermal equilibrium [64].

Although ξ^* and γ^* are predicted separately, their scaling exponents, ν in Eq. (15) and μ in Eq. (16), are found to be related through the Widom hyperscaling relationship [24]:

$$\mu = (d-1)\nu. \qquad (18)$$

Equation (18) is also satisfied in studies of binary mixtures near the critical point in three-dimensional (Euclidean dimension, $d = 3$) systems [62,65-67], where the scaling exponents take the values $\mu = 2v = 1.26$. These exponents belong as well to the 3D Ising universality class [68-70]. The scaling exponents for the 2D and Q2D systems studied here are estimated through power laws as $T \to T_C$, such that, for any variable f, $f(t) \sim t^k$, with $t = 1 - T/T_C$ and $k = lim_{t\to 0} log[f(t)]/log[t]$ [60]. Corrections to scaling terms due to finite size and temperature deviation from T_C, are not pursued because all systems are made sufficiently large and the analysis from which the scaling exponents are calculated is performed near $t = 0$ [25]. Thus, the scaling exponents ν and μ can be expressed as given by Eqs. (15) and (16), respectively. To obtain the scaling exponents, the correlation length and the line tension are plotted as functions of the reduced temperature. Then, ν and μ are extracted from the best fit to the power law [60]. The main panels in Figs. 2a) and 2b) show the results obtained for the normalized correlation length (ξ^*/ξ_0^*) and the normalized line tension (γ^*/γ_0^*), respectively, as functions of T^*/T_C^*, for both 2D and Q2D systems with $a_{ij} = 100$ and $a_{ij} = 140$. Furthermore, Fig. 2 presents a comparison between the results obtained in this work with data [insets in Figs. 2a) and 2b)] from experiments reported by Honerkamp-Smith and collaborators [71]. They measured line tensions and correlation lengths of lipid membranes near critical points, and then extracted their scaling exponents. It is found that the qualitative trends of our simulation data are similar to those reported in the experiments by Honerkamp-Smith *et al.* [71]. On the other hand, the scaling exponents, $\nu = \mu = 1 \pm 0.2$, predicted by our 2D and Q2D simulations are in good agreement with the results of biophysical experiments, where the scaling exponents for the line tension and correlation length in Q2D are obtained [71-73]. To find the statistical average of the scaling exponents $\nu = \mu = 1 \pm 0.2$ (see Eqs. (15) and (16), respectively), all

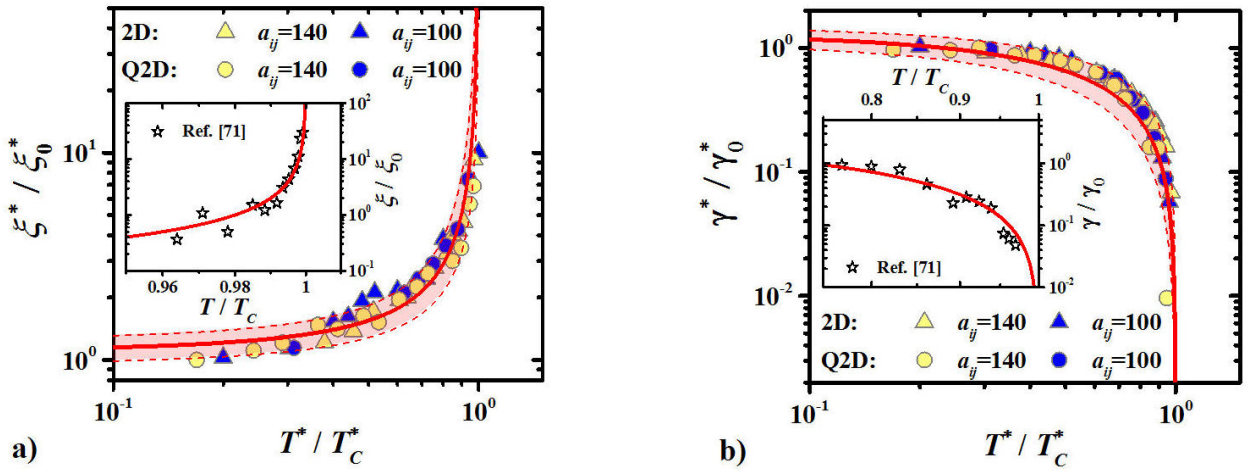

FIGURE 2. Temperature dependence of the normalized correlation length (ξ^*/ξ_0^*) a) and the normalized line tension (γ^*/γ_0^*) b), as functions of the normalized temperature (T^*/T_C^*). The main panels in a) and b) show the results from the simulations of 2D and Q2D binary systems (triangles and circles, respectively). The insets in both panels show some experimental data by Honerkamp-Smith *et al.* [71]. The red curves in a) are allometric functions such that: $\xi^*/\xi_0^* \sim (1 - T^*/T_C^*)^{-v}$; whereas for continuous lines, $v = 1$, and for dashed lines in the main panel, $v = 1 \pm 0.2$. For the main panel of b), the red curves are functions of the form $\gamma^*/\gamma_0^* \sim (1 - T^*/T_C^*)^{\mu}$ with $\mu = 1$ and $\mu = 1 \pm 0.2$, for continuous and dashed curves, respectively. Our simulation data fits are made for $1 - T^*/T_C^* < 0.2$, focusing on values close to T_C^*. For the inset in b) $\mu = 1.2$ [71]. The axes of the main panels are in reduced units, indicated by asterisks. Figures adapted from [25].

data are plotted as single functions $\xi^*/\xi_0^*(t)$ and $\gamma^*/\gamma_0^*(t)$. Subsequently, the functions $\xi^*/\xi_0^*(t) \sim a_\xi t^{-\nu}$ and $\gamma^*/\gamma_0^*(t) \sim b_\gamma t^{\mu}$ are fitted for $t < 0.2$ at temperatures close to T_C^*.

In summary, two major findings are notable for this case study: Widom's hyperscaling relationship is fulfilled not only for 2D systems but also for Q2D systems. This conclusion is important, since experiments are never carried out in strictly 2D but in Q2D. This conclusion is supported by data obtained from Q2D lipid membranes [71]. Secondly, the exponents predicted from simulations under the 2D and Q2D geometry agree with critical exponents of the 2D Ising model, $\nu = \mu = 1$ [24,68], thereby showing that both systems belong to the same universality class.

4.2. Q2D classical Coulomb gas

In this section, the dependence on temperature and on an external magnetic field in the structural and dynamic properties of a classical Coulomb gas with Q2D geometry are presented. The motivation for studying this problem stems from the fact that charged disks in strictly 2D are known to undergo a topological phase transition, from a low temperature condensed state to a high temperature disordered phase. This transition, known as the Kosterlitz-Thouless (KT) transition, occurs at a given critical temperature when the electrostatic interaction between disks is $U(r) \sim \ln(r)$, as is required in strictly 2D [8]. In Q2D, the electrostatic interaction acquires its usual form, $U(r) \sim 1/r$, thus the question arises as to whether the KT transition still takes place under Q2D conditions. To answer this question, we model a low-density gas of highly confined charged spheres. The reduced value for the charges, $|q^*| = 4$, is chosen following previous work on a low density, unmagnetized Coulomb gas in Q2D [44], as it yields a critical temperature (T_C^*) that is sufficiently far from zero ($T_C^* > 0$) to be accurately determined by numerical simulations. The magnitude of the charge can, of course, be chosen as $|q^*| < 4$ but then T_C^* decreases towards zero, as predicted by KT [8], where thermal fluctuations in the system are about the same order of magnitude as T_C^*. This makes it difficult to predict T_C^* accurately without resorting to the exceedingly long simulation times that systems at relatively low temperatures require [44].

An increasing external magnetic field B (defined in Sec. 2) is applied perpendicularly to the plane on which the charged particles move, at fixed temperature, (see Figs. 3(a) and 3(b)). It has been shown that a Q2D Coulomb gas undergoes a topological phase transition at critical temperature $T_C^* = q^{*2}/4r_c^*$ [44], which is invariant under changes in the magnetic field applied. The predicted T_C^* in Q2D is found to be in remarkable agreement with that predicted by the KT theory [8] and confirmed by further numerical simulations for disks in 2D [74]. The caption of Fig. 4 describes how T_C^* is estimated; henceforth all temperatures are normalized by T_C^*.

The structure of the gas is explored by means of the RDFs between opposite charges. Calculating the RDFs allows one to track structural changes in the Q2D Coulomb gas as the temperature increases because it undergoes a topological phase transition, as opposed to an ordinary, first or second order phase transition, for example. The low (below T_C^*) temperature phase displays short range order that reveals itself as peaks in the RDFs at short distance. However, the qualitatively crucial difference with ordinary condensed matter is found in the long-range behavior of the RDFs. For topological phase transitions, as the one reported here for a Q2D Coulomb gas, the long range of the RDFs decays algebraically in the condensed phase and exponentially in the disordered one [8,44]. Tracking the changes in the RDFs with increasing temperature reveals how clustered dipoles uncouple as a consequence of the proliferation of topological defects, which start appearing in the form of unpaired charges. These defects are individual positive or negative charges that progressively decouple with increasing temperature from the condensed structure at temperatures below T_C^*. As temperature increases, thermal fluctuations overcome the binding electrostatic energy of these pairs, leading to the unbinding of dipoles into free charges, an essential feature of the topological phase transition found in Q2D charged spheres.

It is of paramount importance to highlight that a topological phase transition is found to take place in a Q2D Coulomb gas, interacting with the $U \sim 1/r$ electrostatic potential, bearing strong resemblance with the KT phase for disks interacting via the $U \sim -\ln(r)$, 2D electrostatic potential. Here, the potential $U^E(r^*) \sim 1/r^*$ is used to model the electrostatic interactions because, under this Q2D geometry, the systems are made of spheres moving in a box with thin but finite thickness. They are not disks with only two degrees of freedom. Gama Goicochea and Nussinov [44] were the first to find a topological phase transition using the 3D Coulomb interaction, with the critical temperature given exactly by the KT prediction for disk with logarithmic interactions, namely, $T_C^* = q^{*2}/4$ [8]. Moreover, for the Q2D system the spatial correlations in the condensed phase decay algebraically, with a temperature dependent exponent, while they decay exponentially above T_C^*, in agreement with KT [44]. Furthermore, a maximum in the specific heat is found at T_C^*, which is also in agreement with the KT predictions [8]. The influence of the magnetic field **B** on the structure of the fluid, on its translational order parameter (TOP) and on its self-diffusion coefficient D is predicted, to compare our results with those from the literature for strictly 2D systems.

Let us start with the structural analysis of the Q2D Coulomb gas using the spatial correlations between oppositely charged spheres. Figures 3(a) and 3(b) show the RDFs $g(r)$ of two typical Q2D charged sphere systems at $T^* < T_C^*$ and $T^* > T_C^*$, respectively. For simplicity, only results with $B_z^* = 0.0$ and $B_z^* = 0.1$ are shown. The spatial correlations between opposite charges at temperatures lower than T_C^* display algebraic decay, $g(r^*) \sim r^{*-1.1}$ [dashed black line in Fig. 3a)]. The RDFs display sharper oscillations when stronger magnetic field is applied, although the algebraic decay remains unaffected, regardless of the intensity of the ex-

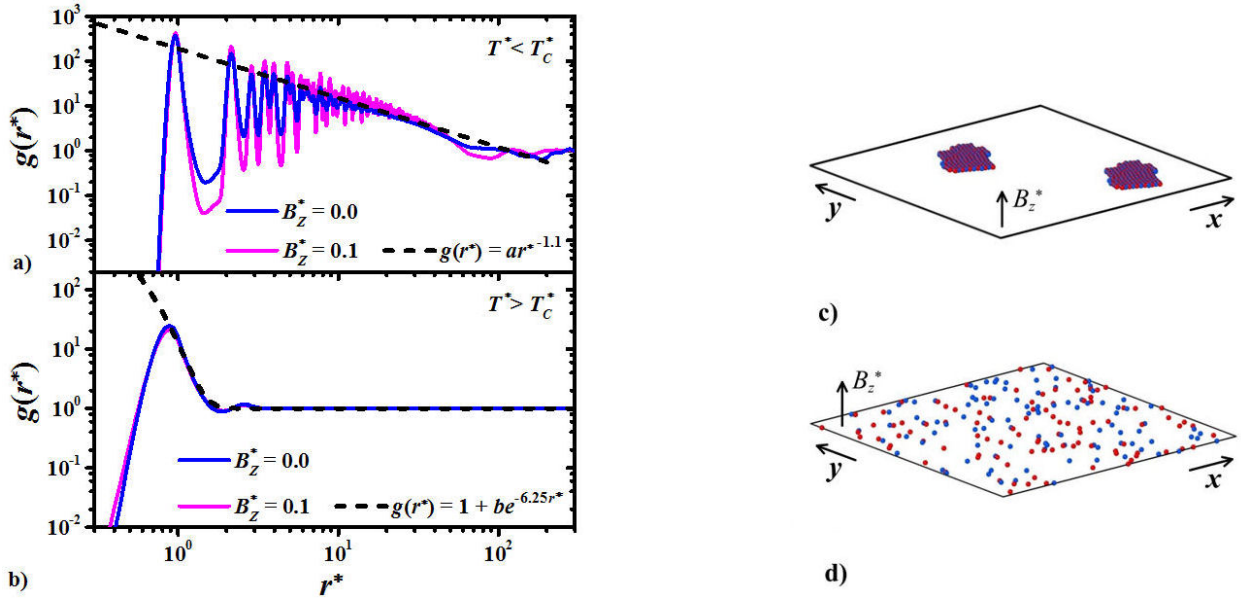

FIGURE 3. a) Radial distribution functions (RDFs) between charges with opposite sign, in the absence of external magnetic field, $B_z^* = 0.0$, and under magnetic field $B_z^* = 0.1$, at $T^* = 0.75 T_C^*$. c) Snapshot of the Q2D Coulomb gas under the external magnetic field $B_z^* = 0.1$ at $T^* = 0.75\ T_C^*$. b) and d) are analogous to a) and c), respectively, for a Q2D Coulomb gas at $T^* = 7.5\ T_C^*$. The black dashed curves in a) and b) indicate the algebraic and exponential decaying trend found for systems with temperatures below and above T_C^*, respectively. The asterisked quantities in panels a) and b) are reported in reduced DPD units. Figures adapted from [26].

ternal magnetic field. These results are in agreement with the predictions for strictly 2D charges [8]. For temperatures above T_C^*, the charged spheres dissociate and their spatial correlations exhibit exponentially decaying RDFs, $g(r^*) \sim e^{-6.25r^*}$ [dashed black line in Fig. 3b)], as in the strictly 2D KT transition [8]. Additionally, they are unaffected by the applied magnetic field. These results show that the structure of the Q2D Coulomb gas is insensitive to the application of an external magnetic field at temperatures below and above T_C^*. This conclusion is consistent with the Bohr-van Leeuwen theorem [75], which states that, if the Hamiltonian of a system in equilibrium is subject to an external magnetic field, its partition function is unaltered by the field. These results agree with previous molecular dynamics simulations for strictly 2D Coulomb gases under transversal magnetic field [76,77].

Additional information on the structural changes taking place in this topological transition is extracted from the calculation of the translational order parameter (TOP) as a function of temperature. The TOP is calculated as follows [28]:

$$\Psi = \frac{1}{N}\left\langle \left| \sum_{j=1}^{N} e^{i\mathbf{K}\cdot\mathbf{r}_j^*} \right| \right\rangle, \tag{19}$$

where N is the total number of particles, K is the first-shell reciprocal lattice vector; the angular brackets indicate average over time. The TOP is predicted in the temperature range $0.375\ T_C^* \leq T^* \leq 11.140 T_C^*$, where T_C^* is defined as the temperature where Ψ_T drops abruptly [44]. This procedure is carried out for all systems under the influence of the external magnetic field, in the range $0.0 \leq |B| \leq 0.1$. In Fig. 4(a), the TOP is shown as a function of reduced temperature, T^*/T_C^*. Below T_C^*, the charges are condensed into a single, Q2D cluster with $\Psi_T \sim 0.9$, which is unchanged by the increased transversal magnetic field. This is expected, of course, since the condensed phase is an agglomerate with net charge equal to zero, thus a magnetic field should exert no force on it. Above T_C^*, the condensed phase begins to melt and the charges become increasingly unpaired, yielding a TOP close to zero ($\Psi_T \sim 0.07$). The results for the TOP reveal that once the temperature exceeds T_C^*, Ψ_T displays increased sensitivity to temperature. Data in Fig. 4(a) show that below T_C^*, the TOP standard deviation is less than $\sim 8\%$, with one exceptional case for the unmagnetized system at $T^* = 0.454 T_C^*$ showing a standard deviation of $\sim 13\%$. Then, near $T^*/T_C^* = 1$, the statistical deviations of the TOP increase up to $\sim 52\%$. The increased uncertainty in the calculated values of the TOP for $T^*/T_C^* > 1$ but close to T_C^*, is due to the gradual breakdown of dipolar correlations. As thermal fluctuations intensify just above the T_C^*, unpaired charged spheres begin to proliferate, reducing the signal to noise ratio in the calculation of the TOP, which translates into larger error bars.

The dynamic behavior of the Q2D low-density, classical Coulomb gas is explored through the self-diffusion coefficient, D^*, which is obtained from the mean-square displacement of the N charged particles [80]:

$$D^* = \frac{1}{6tN}\left\langle \sum_{i=1}^{N} |\mathbf{r}_i(t) - \mathbf{r}_i(0)|^2 \right\rangle. \tag{20}$$

The self-diffusion coefficient D^* is then calculated as a function of $\beta^* = \omega_C^*/\omega_P^*$ and $\Gamma^* = q^{*2}/aT^*$. Here, β^* is

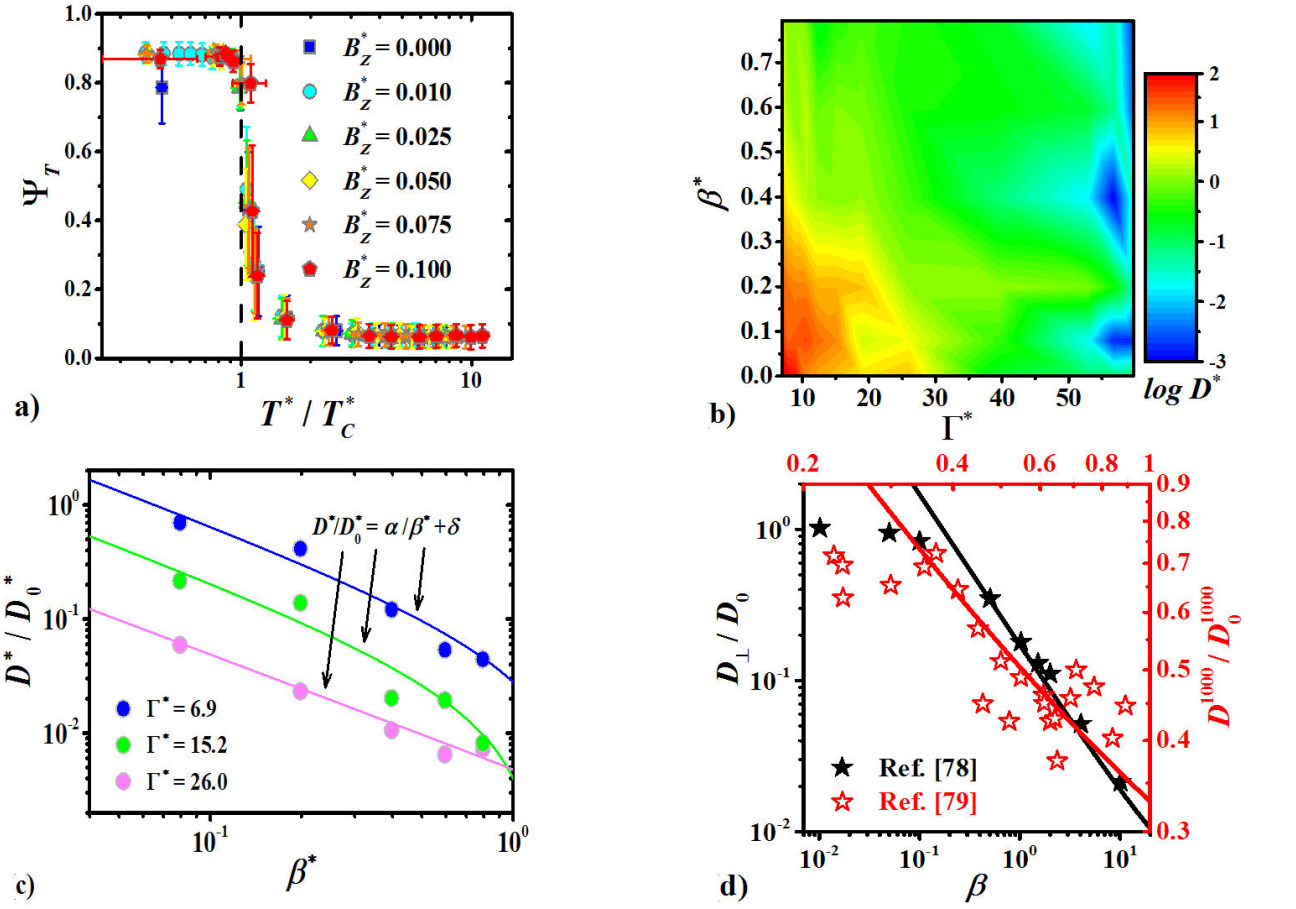

FIGURE 4. a) Translational order parameter (Ψ_T) as a function of the normalized temperature T^*/T_C^* for increasing transverse magnetic field B_z^*. The vertical dashed line indicates where $T^*/T_C^* = 1$, with $T_C^* = q^{*2}/4r_c^*$. b) Map of the self-diffusion coefficient D as a function of the parameter $\beta^* = \omega_c/\omega_p$ and the coupling constant Γ^*; the intensity of D is shown on logarithmic scale for clarity (see color bar in b)). c) Normalized self-diffusion coefficient (D^*/D_0^*) as a function of β^* parameter, for three values of Γ^*, at $T^*/T_C^* > 1$ in all cases. The solid black stars in d) are data from MD simulations reported by Vidal and Baalrud [78], while the empty red stars are data taken from reference [79]; see the text for details. The solid lines in panels c) and d) are best fit to the Bohm diffusion mode, where $D^*/D_0^* = \alpha/\beta + \delta$, with α and δ being fitting parameters. All units marked with asterisks refer to reduced units.

the ratio of the cyclotron frequency ($\omega_C^* = q^*\, B_z^*/m^*$) and the plasma frequency ($\omega_P^* = \rho^* q^{*2}/\varepsilon_0 m^* a$), with m being the mass of the charged particle, ρ^* the reduced density of the gas, and ε_0 the vacuum permittivity. Γ^* is the plasma coupling constant, with $a = (4\pi\rho^*/3)^(1/3)$ being the Wigner-Seitz radius. The dependence of D^* on β^* and Γ^* is shown in Fig. 4b) in the form of a heatmap, where "cold" and "warm" colors refer to low and high self-diffusion coefficients, respectively. The diffusion of the particles is higher, by about three orders of magnitude, when the systems are under relatively high temperatures (low values of Γ^*). However, the high mobility of the charges found when the condensed phase melts is strongly suppressed by the increasing magnetic field. This effect can be understood by the fact that when charges are unpaired, they couple to the external magnetic field, which imparts circular motion in them, resulting in the reduction of their mean displacements over the plane transversal to the field direction. Further analysis of the self-diffusion coefficient as a function of increasing magnetic field is provided in Fig. 4c), where the normalized diffusion coefficient D^*/D_0^* vs β^* is shown. D_0^* is the value of the self-diffusion coefficient of the unmagnetized system at $T^*/T_C^* = 7.5$. It is found that the charges' diffusion follows the so-called Bohm diffusion mode [81], where D^* goes as $\sim 1/\beta^*$. This type of diffusion has also been identified in several 2D and Q2D one-component plasmas (OCP) studied via MD simulations [14,78,79,82,83] and experimentally [79].

The results reported here for a low-density, Q2D Coulomb gas modeled at the mesoscale, are compared with some results obtained by two different groups, shown in Fig. 4d). Vidal and Baalrud [78], who study the self-diffusion behavior of strongly magnetized OCP via MD simulations, find that the component of the diffusion coefficient that is perpendicular to the magnetic field ($D_\perp$), which is a strictly 2D property, scales as $D_\perp \sim \beta^{-1}$ for strongly magnetized OCP systems (following criteria established by Baalrud and Daligault [84]). Black stars shown in Fig. 4d) are data from

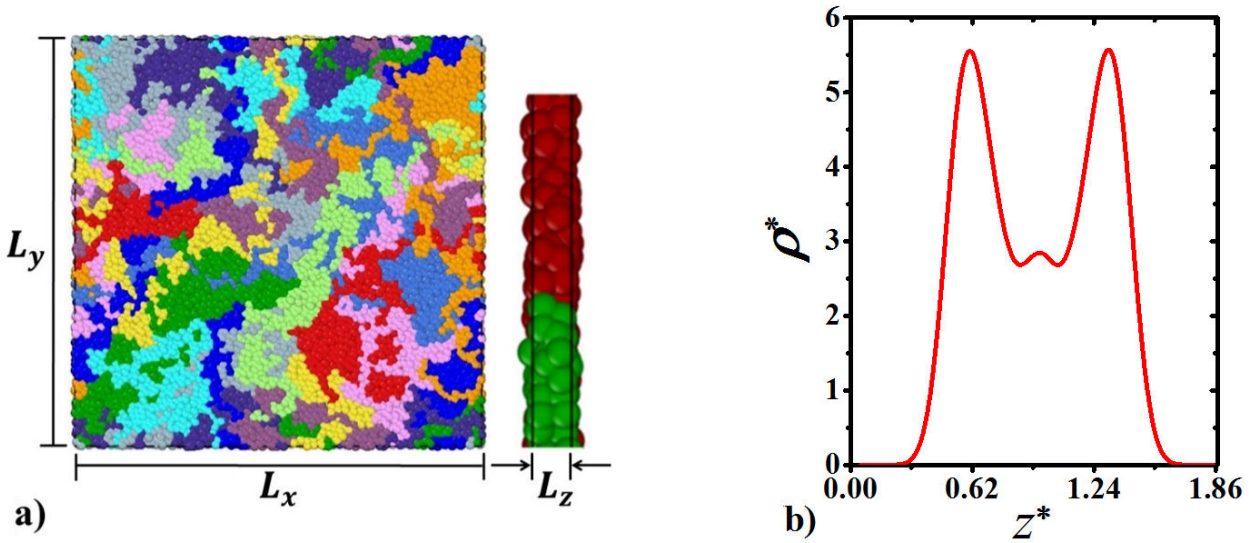

FIGURE 5. a) Top-view snapshot and a lateral close-up (to highlight the Q2D nature of the geometry) of the polymer melt with $N = 1000$ and $c^* = 2.1$. Each chain is depicted with a different color, for clarity; $L_z = 1.87$. b) Reduced density profile a typical system of $c^* = 2.1$ along the z-direction.

data from Fig. 5c) in Ref. [78], corresponding to an OCP of $N = 5 \times 10^3$ particles with coupling parameter $\Gamma = 10$. On the other hand, experiments on quasi-magnetized dusty plasmas in 2D carried out by Hartmann and colleagues [79], have shown that for $\beta \sim 1$, the relative diffusion coefficient (D^{1000}/D_0^{1000}) exhibits Bohm's diffusion. Here, D^{1000} refers to a fixed-time coefficient such that $t = 1000/\omega_P$, while the D_0^{1000} values are obtained through MD simulations since in that particular experiment, Γ cannot be set arbitrarily. In Fig. 4(d), red stars are data from experiments taken from Fig. 6 of Ref. [79], where the values Γ for all data are in the range of $18.3 \leq \Gamma \leq 124.0$.

4.3. Q2D polymer melts

The last case study presented here focuses on a novel scaling law put forward for the osmotic pressure (Π) of Q2D dense polymer melts [27]. Here, the osmotic pressure of the systems is computed as the difference between the component of the pressure tensor normal to the confinement direction, *i.e.*, z-direction, and the bulk pressure, such that: $\Pi^* = \langle P_{zz} - P_{\text{bulk}}$. The bulk pressure, P_{bulk}, is taken as the pressure of the unconfined DPD fluid, which is obtained from the DPD equation of state, $P_{\text{bulk}} = \rho^* k_B T^* + \alpha a_{ii} \rho^{*2}$, where $4\alpha = 0.101$, and a_{ii} is defined by Eq. (4) [30]. The z-component of the pressure tensor is $\langle P_{zz} \rangle = \langle \sum_i m_i^* \mathbf{v}_{iz} \cdot \mathbf{v}_{iz} + \sum_i \sum_{j>i} f_{ij\,z}^C z_{ij}^* \rangle / V$, where the first term in the right-hand side of the equation is the ideal gas contribution, and the second term is the so called "excess pressure" contribution [28]. The force $f_{ij\,z}^C$ is the z-component of the total conservative force between the i-th and j-th particles, including non-bonding DPD, harmonic spring between beads, and effective wall forces [28]. The angular brackets refer to averages over time. Panel (a) in Fig. 5 displays a top-view snapshot of a typical polymer melt system (with polymerization degree of $N = 500$ at concentration of $c^* = 2.4$) under Q2D geometry. The structure of the fluid is additionally studied using the information in panel (b), which is the density profile along the direction of strong confinement. It shows one polymers' layer near each of the confinement walls at $z^* = 0$ and at $z^* = L_z = 1.87$.

It is well-known that some static and dynamic properties of polymers can be understood through simple scaling laws [85]. Such is the case with the radius of gyration (R_G), which under good solvent conditions scales with the polymerization degree (N) as $R_G \sim N^v$ [85,86], where Flory's exponent is $v \approx 3/5$ [87] in 3D and $v = 3/4$ [85] in 2D. Recently, we introduced a fractal scaling law for the osmotic pressure of polymer melts [27]:

$$\Pi \sim c^{*2vd_f/2vd_f-1}, \tag{21}$$

where d_f is the fractal dimension associated with polymers' contour length, L^*. This expression is obtained for polymer melts under two key conditions. The first comes from the work of Semenov and Johner [9], who showed that the relevant length scale in dense 2D polymer melts is no longer the radius of gyration but the contour length. The latter scales as $L \sim R_G^{d_f} \sim N^{vd_f}$, yielding a renormalization of the characteristic blob size such that $\xi \sim L(c/c^{*'})^{\beta}$. The exponent β is chosen so as to make ξ independent of N; for further details, see [27]. The second condition is that there exists a critical concentration ($c^{*'}$) at which the interchain monomer concentration of the melt equals the intrachain monomer concentration of the 2D polymer chains, where $c^{*'} \sim N/L^d$, with $d = 2$ being the Euclidean dimension. Thus, following the scaling arguments stated by des Cloizeaux [88] and de Gennes [85] for semidilute polymers –where the dilute-to-semidilute transition occurs at the critical concentration, $c^* \sim N/R_G^d$ - one assumes that $\Pi \sim (c^*/N)\,(c^*/c^{*'})^m$.

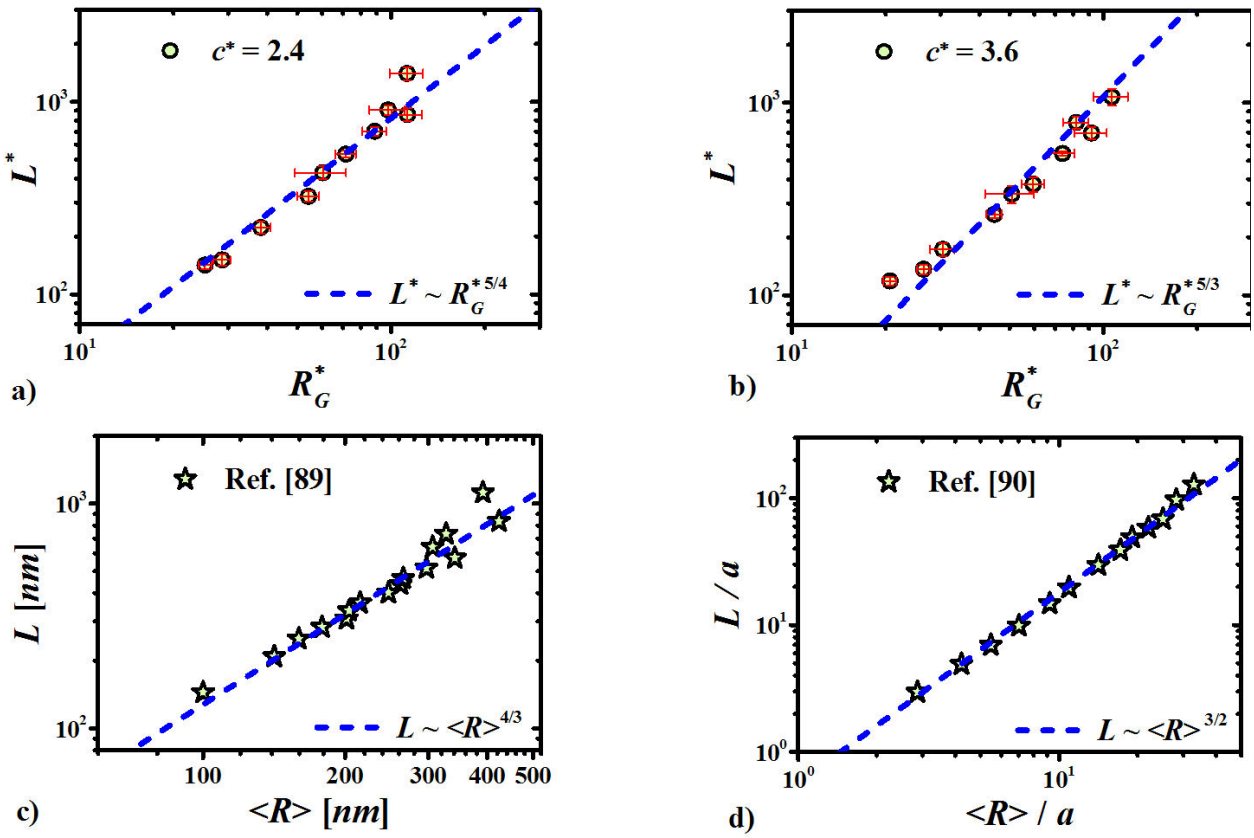

FIGURE 6. Correlation between the polymers' contour length, L^*, and their radius of gyration, R^*_G, for some chosen concentrations: a) $c^* = 2.4$ and b) $c^* = 3.6$. c) Experimental data for dense layers of bottle brush polymers in Q2D, by Gallyamov and collaborators [89]. d) Experimental results reported by Wang and Foltz [90] for Q2D, dense diblock copolymers, where the thickness of the monolayer formed by the copolymers is $a \approx 20$ nm. The different fractal dimension d_f regimes stated by the scaling relation $L^* \sim R_G^{*d_f}$, are depicted by the blue dashed lines -taking into account that polymers' end-to-end distance R is proportional to R_G. The axes in panels a) and b) are in reduced DPD units.

Then, choosing the exponent as $m = 1/(2vd_f - 1$ so as to make Π independent of N when $c^* > c^{*'}$, yields the expression in Eq. (21).

Before testing Eq. (21), we start by showing that the polymer melts studied here are indeed in the dense regime. To prove this claim, Fig. 6a) shows the polymers' contour length as a function of the radius of gyration, to test Semenov and Johner's postulate that $L^* \sim R_G^{*d_f}$, with $d_f = 5/4$ being the first fractal dimension found in the semidilute-to-melt transition [9,27] However, our results reveal that transitions between increasing fractal dimensions take place as the concentration increases, with d_f growing monotonically so that $d_f \to 2$ as c^* approaches the saturation concentration. This conclusion should be expected since the voids present in the 2D polymer melt are systematically filled as c^* grows, making the contours of all polymers more irregular, or fractal. To test these findings, some experimental results of Q2D dense polymer systems, taken from the literature, are displayed in Fig. 6c) and 6d). Data in Fig. 6c) are taken by Gallyamov *et al.* [89], who measured the contour lengths of bottle-brush polymers confined in films with thickness $\sim$ 10 nm, finding that $L \sim \langle R\rangle^{4/3}$. Results from Wang and Foltz [86] are shown in Fig. 6d), who find that the contour length of dense polybutadiene and polystyrene block copolymers in films with thickness $\sim$ 20 nm scales as $L \sim \langle R\rangle^{3/2}$.

The fractal transitions predicted from the polymers' contour length analysis above are supported by the results obtained for the Q2D osmotic pressure as a function of the monomer concentration, for a wide range of polymerization degree values -up to N=4000. The results are shown in Fig. 7a), which confirm the scaling law presented in Eq. (21). Fractal dimension transitions are indicated in Fig. 7a) by monotonically decreasing exponents in $\pi(c^*)$, as c^* is increased. They start at $\Pi \sim c^{*5}$, with $d_f = 5/4$ being the first fractal dimension expected in the semidilute-to-melt transition [9,27]. This first fractal regime is followed by continuous increase of fractal dimensions, reaching eventually $d_f = 2$, which corresponds to $\Pi \sim c^{*2}$ at the maximum concentration, as predicted by Eq. (21). These transitions take place continuously as the concentration increases. However, for clarity only four of those are displayed in Fig. 7a), representing $d_f = 5/4$, 4/3, 3/2 and 2 (*i.e.*, $\Pi \sim c^{*5}$, $\Pi \sim c^{*4}$, $\Pi \sim c^{*3}$ and $\Pi \sim c^{*2}$, respectively); see the differently colored solid lines in Fig. 7a). Although fractal scaling was pre-

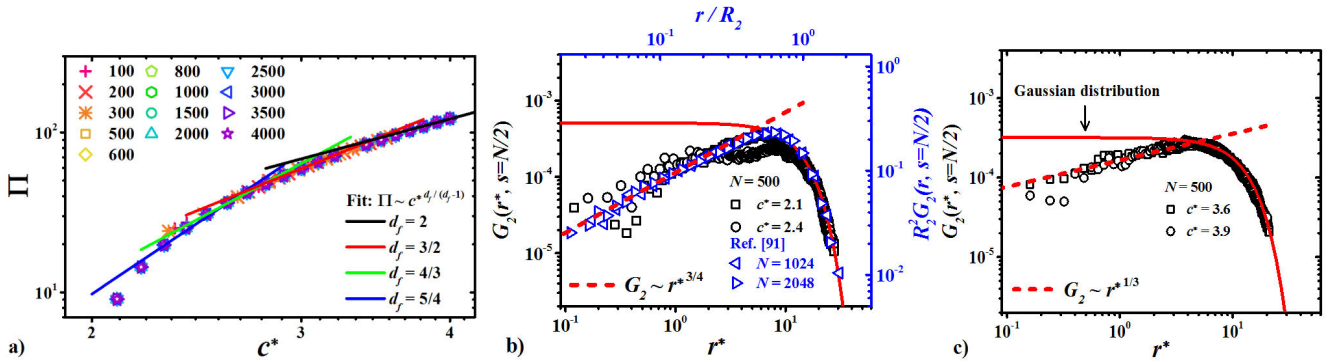

FIGURE 7. a) Osmotic pressure (Π) of the Q2D polymer melts, as a function of the monomer concentration c^* for chains with different polymerization degrees, N. The solid lines indicate the different fractal regimes as c^* is increased; see Eq. (21). Panels b) and c) are the RDFs between the inner monomer segments s of polymers with $N = 500$, for a characteristic set of concentrations belonging to the fractal regimes with $d_f = 5/4$ and $d_f = 5/3$, corresponding to exponents $\Theta_2 = 3/4$ and $\Theta_2 = 1/3$, respectively (see Eq. (23)). The fractal regime found herein for relatively low concentrations [black data in panel a)] agrees with results reported by Meyer and co-workers [91] [blue data in panel a)]. The monomers at the ends of each polymer were excluded from our RDF calculations; see main text. The solid lines in b) and c) represent the Gaussian distribution of an ideal chain in 2D, $y = \exp(-x^2)/\pi$. The dashed lines in b) and c) are the best fits to the function $G_2 \sim r^{*\Theta_2}$. The asterisks refer to reduced units.

dicted scaling was predicted originally for strictly 2D systems and only for $d_f = 5/4$ [9], here it is shown that it also appears in Q2D polymer melts under strong confinement, and for a continuous range of values in [5/4,2].

In a previous study of strictly 2D polymer solutions carried out by Schulmann and colleagues [18], the semidilute-to-melt fractal transition in the pressure was found as well, in agreement with our predictions [27]. They find that the pressure (βP, with $\beta = 1/k_B T$) at relatively low concentrations ($\rho < 0.5$) scales as $\beta P \sim \rho^3$, as expected for the semidilute regime in 2D [85]. However, as they increase the polymer concentration, their data reveal a fractal transition such that, for $\rho > 0.5$, the pressure then scales as $\beta P \sim \rho^5$, corresponding to $d_f = 5/4$; see Eq. (21) and recall $v = 0.5$ in the melt. Although they did not carry out such analysis for $\rho > 0.5$ [18], the pressure data they report fit the universal fractal scaling for dense Q2D polymer melts introduced in the present work.

An additional independent test carried out in this study confirms the fractal transitions that the Q2D polymer melts undergo in the dense regime, predicted by Eq. (21). This is accomplished with the calculation of the RDF between the inner segments of monomers of each polymer chain of size s, known as $G_2(r^*, s)$. The function $G_2(r^*, s)$ is calculated as the segment distribution function of size, $s = N/2$. Since r^* is the characteristic distance between the i-th and j-th monomers forming the segment $s = N/2$ within the m-th polymer, $G_2(r^*, s)$ is calculated as a typical $g(r^*)$ [28], without taking into account the end monomers of the polymers, as follows:

$$G_2(r*, s = N/2) = \left\langle \frac{1}{m} \sum_m \left(\sum_{i=2}^{s-1} \sum_{\substack{j=i+s \\ j-i=s}}^{2s-1} g(r*) \right) \right\rangle, \quad (22)$$

where the angular brackets represent the ensemble average, corresponding to the production phase of the simulations. Duplantier [92] and des Cloizeaux [88] state that the RDFs of the average contacts between monomers of each chain go as $G(r) \sim r^{\Theta}$, for self-avoiding walks. The exponent associated with the probability of contacts between inner monomers exclusively is denoted by Θ_2; whereas Θ_1 is for contacts between the chain's ends and inner monomers within a single chain, and Θ_0 applies for contacts between the chain's ends. Meyer and co-workers showed that the exponent Θ_2 is related to the fractal dimension as follows [91]:

$$d_f = d - \Theta_2, \quad (23)$$

where $d = 2$ is the Euclidean dimension. Figures 7b) and 7c) display the RDFs, $G_2(r^*, s = N/2)$, of polymer melts with $N = 500$ at four monomer concentrations, with two of them at relatively low values of c^* (Fig. 7b)) and two at relatively high values of c [Fig. 7c)]. Our data for low concentrations (black symbols) are compared with those from Meyer et al. [91] (blue symbols), in Fig. 7b). The same $\Theta_2 = 3/4$ exponent is found as the first fractal regime takes place, corresponding to $d_f = 5/4$, just as Duplantier predicts [92]. Other researchers have found the same exponent through numerical simulations for strictly 2D objects [18,93]. However, our findings go beyond this first fractal regime. We have found that the fractal transitions predicted from the contours' length and osmotic pressure analyses also emerge from the inner structure of dense polymer melts. It is observed that, as c^* is increased the probability of contacts between the inner monomers ($P \sim G_2 \sim r^{*\Theta_2}$) becomes larger. This occurs because inner monomers are mostly surrounded by other inner monomers of the same chain for increasing monomer concentration, especially when those chains possess a large polymerization degree. The structure of the polymer melt is continuously modified with c^*, since any voids present are filled with more monomers as c^* increases, which reduces the exponent Θ_2. Such feature is seen in Fig. 7b), where a clear

reduction in the contact exponent to $\Theta_2 = 1/3$ is obtained, leading to $d_f = 2/3$ when $c^* \geqslant 3.6$.

5. Conclusions

A short review of three physical systems under quasi-two-dimensional (Q2D) geometry that follow laws derived for strictly 2D system is presented. The first case study, concerned with the prediction of the line tension between two immiscible fluids and their correlation length in Q2D, showed that the line tension obeys scaling laws derived for 2D disks. The second case study regards highly confined charged spheres in a low density gas that displays a topological phase transition as the temperature changes, found to be closely related to its strictly 2D counterpart, which is the well-known Kosterlitz-Thouless transition. The last case focuses on dense, Q2D long polymer melts whose osmotic pressure obeys a novel fractal scaling law developed by the authors, which is backed by experiments and numerical simulations from other groups. The results highlight the robustness of the scaling concept and statistical thermodynamics models, developed originally for strictly 2D systems, in the correct prediction of physical properties of Q2D systems. This claim is supported by scaling laws and theories developed for strictly two dimensional systems, as is the case for Widom's hyperscaling relation [24,25] and for the Kosterlitz-Thouless topological phase transition [8,26,44]. It is also supported with the test in Q2D materials of a fractal scaling law recently proposed by the authors for the osmotic pressure of dense polymer melts [27]. The work reported here is not an academic exercise but rather a conclusion whose importance cannot be overstated, since all 2D materials synthesized and probed experimentally are actually Q2D materials. These results are expected to inspire further investigations in branches of nanoscience where Q2D models of single, binary, or complex fluids are of interest to gain fundamental understanding of nature.

Appendix

A. Methodology used to calculate the spatial correlation length (ξ^*)

A.1 Calculation of ξ^* using the radial distribution function

The spatial correlation length between the two immiscible phases (ξ^*) can be estimated through the radial distribution function between the water and oil particles (water-oil RDF), specifically using the fist derivative of the water-oil RDF, $g'(r^*)$. To illustrate the methodology, in this Appendix the case shown in Fig. 1f) is used, which is the Q2D system with interaction parameter $a_{ij} = 140 k_B T^*/r_c^*$ at the reduced temperature $t = 0.702$. Fig. 8 shows the water-oil RDF (inset in Fig. 8) and its first derivative, which represents the slope

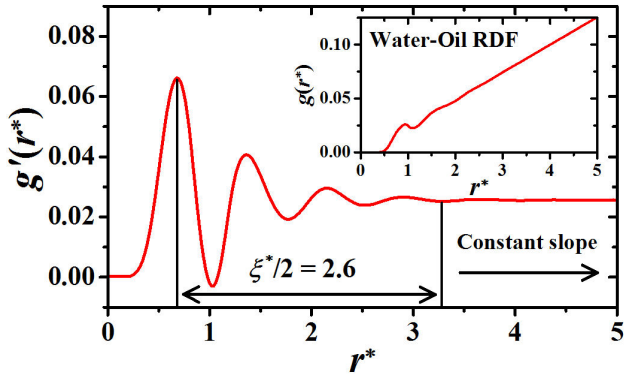

FIGURE 8. Derivative of the radial distribution function between water and oil particles, $g'(r^*)$, for a Q2D system with $a_{ij} = 140 k_B T^*/r_c^*$ at reduced temperature of $t = 0.702$. The vertical lines indicate the position of the first maximum and the last minimum of $g'(r^*)$, where the separation between them is defined as $\xi^*/2$. The inset shows the water-oil RDF of the same system.

of the function $g(r^*)$. The water-oil RDF of a well-formed interface shows structure at relatively short distances because only the particles within the interfacial region respond to the structure due to the other phase, having an intrinsic width, ξ^*. Furthermore, such a structure is barely noticed in their $g(r^*)$ because the quantity of fluid forming the interface is considerably small if compared with the whole fluid mixture. In this example, the inset in Fig. 8 shows that the fluctuations in the water-oil RDF end at $r^* \approx 2$, although they become unnoticeable around this value. However, the first derivative of $g(r^*)$ allows one to see how the slope changes as a function of the characteristic distance r^* and to compute the distance at which the fluctuations of the function $g(r^*)$ end. Beyond the distance at which the fluctuations of $g'(r^*)$ are negligible, it is constant because the water-oil RDF increases proportionally with r^*. The monotonous increase observed in the function $g(r^*)$ is attributed to the two well-defined phases separated by the interface. From the $g'(r^*)$ in Fig. 8, the distance between the first maximum and last minimum of the function is defined as $\xi^*/2$, since the RDF gives the radial distances. These two points are indicated by the vertical lines in the main panel of Fig. 8 and refer to the relative distances at which the water-oil spatial distribution starts showing the radial structural layering. It is found that the spatial correlation length of the system (the same system shown in Fig. 1 under a Q2D geometry) is $\xi^* = 5.2$.

A.2 Calculation of ξ^* using the density profiles

The spatial correlation length, ξ^*, reported in Fig. 2a), is estimated from the density profiles ($\rho^*(y^*)$; see Fig. 1) averaged over the production stage of the simulations. Using the first derivative of the function $\rho^*(y^*)$, the thickness of the interface is determined, called ξ^*. The criterion used to define the interfacial region is based on the change in the slope of the density profile, $\rho^{*'}(y^*)$. The edge of the interface, of width ξ^*, delimited by the water phase is defined as the position in the y-axis where $\rho^{*'}(y^*)$ shows the first change of 0.05 units,

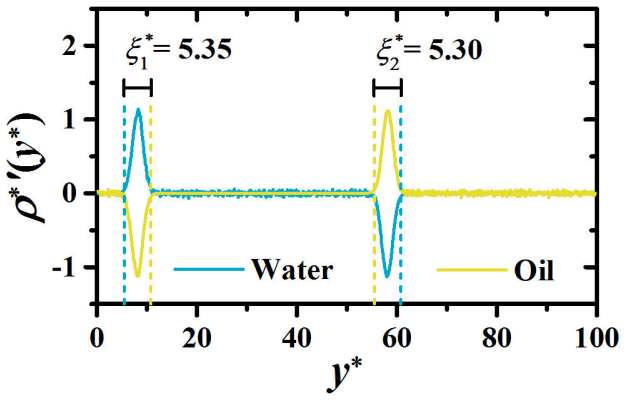

FIGURE 9. Derivative of the density profiles along the y-direction for the Q2D immiscible liquids with interaction parameter $a_{ij} = 140k_BT^*/r_c^*$ at reduced temperature $t = 0.702$. The vertical dashed lines determine the interfacial thickness, *i.e.*, ξ^*; using the criterion described in the main text of Appendix A.

and similarly for the oil phase. This choice is based on the thickness of the slab defined a priori to form the density profiles, which is $\Delta y^* = 0.05$; thus, an increment of $\Delta\rho^{*'}(y^*) = 0.05$ corresponds to the slab width.

Figure 9 shows how to calculate ξ^* using the first derivative of the function $\rho^*(y^*)$ for a system with Q2D geometry and with interaction parameter $a_{ij} = 140k_BT^*/r_c^*$ at the reduced temperature of $t = 0.702$, related to Fig. 1f). The vertical yellow and blue dashed lines indicate the positions at which the oil and water $\rho^{*'}(y^*)$ functions take the value $|\rho^{*'}(y^*)| = 0.05$, respectively. Those positions along the y-axis are phase boundaries and the difference between them is defined as the interfacial width, called ξ^*. If one tracks the function $\rho^{*'}(y^*)$ of the water phase (blue solid curve in Fig. 9) moving in the positive direction along the y-axis, one finds that beyond $y^* = 60.8$ (vertical blue line in Fig. 9) the water phase does not exist anymore. If one moves on the opposite direction along the y-axis, tracking the oil phase function $\rho^{*'}(y^*)$ (yellow solid curve in Fig. 9), it is found that the oil phase ends at $y^* = 55.5$ (vertical yellow line in Fig. 9). The spacing between these two lines indicates the average interfacial width (since $\rho^*(y^*)$ is a function averaged over time), which for this particular case corresponds to $\xi_2^* = 5.3$. Notice that in this example the two interfaces appear in the graphic [as seen also in Fig. 1f)]; the same criterion was applied to find ξ_1^* and ξ_2^*. This procedure is applied to each 2D and Q2D system's density profiles to estimate their interfacial width, *e.g.*, ξ^*.

Acknowledgments

This project was sponsored by CONAHCYT through grant number 320197. JDHV thanks also CONAHCYT for support. The authors are indebted to S. A. Alas, Z. Nussinov, and E. Pérez for insightful discussions.

1. L.P. Kadanoff, Statistical Physics: Statics, Dynamics and Renormalization, (WORLD SCIENTIFIC, 2000). https://doi.org/10.1142/4016.
2. H. Zhang *et al.*, Recent advances of two-dimensional materials in smart drug delivery nano-systems, *Bioact. Mater.* **5** (2020) 1071. https://doi.org/10.1016/j.bioactmat.2020.06.012.
3. H. Huang, W. Feng and Y. Chen, Two-dimensional biomaterials: material science, biological effect and biomedical engineering applications, *Chem. Soc. Rev.* **50** (2021) 11381. https://doi.org/10.1039/D0CS01138J.
4. D. Tyagi *et al.*, Recent advances in two-dimensional-material-based sensing technology toward health and environmental monitoring applications, *Nanoscale* **12** (2020) 3535. https://doi.org/10.1039/C9NR10178K.
5. H. Lin *et al.*, Emerging Low-Dimensional Nanoagents for Bio-Microimaging, *Adv. Funct. Mater.* **30** (2020) 2003147. https://doi.org/10.1002/adfm.202003147.
6. C. Liu *et al.*, Two-dimensional materials for next-generation computing technologies, *Nat. Nanotechnol.* **15** (2020) 545. https://doi.org/10.1038/s41565-020-0724-3.
7. M. E. Fisher, The theory of equilibrium critical phenomena, *Rep. Prog. Phys.* **31** (1968) 508. https://doi.org/10.1088/0034-4885/31/1/508.
8. J. M. Kosterlitz and D. J. Thouless, Ordering, metastability and phase transitions in two-dimensional systems, *J. Phys. C Solid State* **6** (1973) 1181. https://doi.org/10.1088/0022-3719/6/7/010.
9. A. N. Semenov and A. Johner, Theoretical notes on dense polymers in two dimensions, *Eur. Phys. J. E* **12** (2003) 469. https://doi.org/10.1140/epje/e2004-00019-2.
10. M. R. Eustaquio-Armenta, G.A. Méndez-Maldonado and M. González-Melchor, The line tension of two-dimensional ionic fluids, *J. Chem. Phys.* **144** (2016) 134705. https://doi.org/10.1063/1.4944731.
11. S. Toxvaerd, Computer simulation of melting in a two-dimensional Lennard-Jones system, *Phys. Rev. A* (Coll Park) **24** (1981) 2735. https://doi.org/10.1103/PhysRevA.24.2735.
12. J. P. Hansen, D. Levesque and J. J. Weis, Self-Diffusion in the Two-Dimensional, Classical Electron Gas, *Phys. Rev. Lett.* **43** (1979) 979. https://doi.org/10.1103/PhysRevLett.43.979.
13. G. S. Dubey and G. Gumbs, Two-dimensional Coulomb systems in a uniform magnetic field, *Phys. Lett. A* **252** (1999) 67. https://doi.org/10.1016/S0375-9601(98)00919-0.
14. Y. Feng *et al.*, Superdiffusion of two-dimensional Yukawa liquids due to a perpendicular magnetic field, *Phys. Rev. E* **90** (2014) 013105. https://doi.org/10.1103/PhysRevE.90.013105.

15. G. S. Dubey, G. Gumbs and V. Fessatidis, Dynamical properties of magnetized two-dimensional one-component plasma, *Phys. Lett. A* **382** (2018) 1374. https://doi.org/10.1016/j.physleta.2018.03.032.

16. A. Yethiraj, Computer Simulation Study of Two-Dimensional Polymer Solutions, *Macromolecules* **36** (2003) 5854. https://doi.org/10.1021/ma025907r.

17. P. Polanowski, J.K. Jeszka, A. Sikorski, Monte Carlo studies of two-dimensional polymer-solvent systems, *J. Mol. Model.* **23** (2017) 63. https://doi.org/10.1007/s00894-017-3216-0.

18. N. Schulmann *et al*., Strictly two-dimensional self-avoiding walks: Density crossover scaling, *Polym. Sci. Ser. C+* **55** (2013) 181. https://doi.org/10.1134/S1811238213070072.

19. S. Thiel *et al*., Tunable Quasi-Two-Dimensional Electron Gases in Oxide Heterostructures, *Science* **313** (2006) 1942. https://doi.org/10.1126/science.1131091.

20. T. Zhang *et al*., Engineering crystalline quasi-two-dimensional polyaniline thin film with enhanced electrical and chemiresistive sensing performances, *Nat. Commun.* **10** (2019) 4225. https://doi.org/10.1038/s41467-019-11921-3.

21. C. Klopp and A. Eremin, On Droplet Coalescence in Quasi-Two-Dimensional Fluids, *Langmuir* **36** (2020) 10615. https://doi.org/10.1021/acs.langmuir.0c02139.

22. K. S. Novoselov *et al*., Electric field in atomically thin carbon films, *Science* **306** (2004) 666. https://doi.org/10.1126/science.1102896.

23. P. J. Hoogerbrugge and J. M. V. A. Koelman, Simulating Microscopic Hydrodynamic Phenomena with Dissipative Particle Dynamics, *Europhys. Lett*. **19** (1992) 155. https://doi.org/10.1209/0295-5075/19/3/001.

24. B. Widom, Surface tension and molecular correlations near the critical point, *J. Chem. Phys.* **43** (1965) 3892. https://doi.org/10.1063/1.1696617.

25. J. D. Hernández Velázquez and A. Gama Goicochea, Hyperscaling of the correlation length, interfacial tension, and specific heat in two-dimensional and quasi-two-dimensional liquids, *J. Chem. Phys.* **158** (2023) 234702. https://doi.org/10.1063/5.0147786.

26. J. D. Hernández Velázquez, Z. Nussinov and A. Gama Goicochea, Self-diffusion and structure of a quasi two-dimensional, classical Coulomb gas under increasing magnetic field and temperature, *Phys. Rev. Res.* **5** (2023) 043223. https://doi.org/10.1103/PhysRevResearch.5.043223.

27. J. D. Hernández Velázquez, S.J. Alas, E. Pérez and A. Gama Goicochea, Universal scaling of the osmotic pressure for dense, quasi-two-dimensionally confined polymer melts reveals transitions between fractal dimensions, *J. Chem. Phys.* **160** (2024) 084907. https://doi.org/10.1063/5.0185634.

28. M.P. Allen and D.J. Tildesley, Computer Simulations of Liquids (Oxford University Press, New York, 1987).

29. P. Español and P. Warren, Statistical Mechanics of Dissipative Particle Dynamics, *Europhys. Lett.* **30** (1995) 191. https://doi.org/10.1209/0295-5075/30/4/001.

30. R. D. Groot and P. B. Warren, Dissipative particle dynamics: Bridging the gap between atomistic and mesoscopic simulation, *J. Chem. Phys*. **107** (1997) 4423. https://doi.org/10.1063/1.474784.

31. E. Mayoral, A. Gama Goicochea, Modeling the temperature dependent interfacial tension between organic solvents and water using dissipative particle dynamics, *J. Chem. Phys*. **138** (2013) 094703. https://doi.org/10.1063/1.4793742.

32. R. D. Groot and K. L. Rabone, Mesoscopic simulation of cell membrane damage, morphology change and rupture by nonionic surfactants, *Biophys. J.* **81** (2001) 725. https://doi.org/10.1016/S0006-3495(01)75737-2.

33. G. S. Grest and K. Kremer, Molecular dynamics simulation for polymers in the presence of a heat bath, *Phys. Rev. A (Coll Park)* **33** (1986) 3628. https://doi.org/10.1103/PhysRevA.33.3628.

34. J. Santos - Santos, R. Soto - Guzmán, J. D. Hernández Velázquez and A. Gama Goicochea, The importance of angular bending of Gemini surfactants on their encapsulation efficiency, *J. Mol. Liq.* **381** (2023) 121797. https://doi.org/10.1016/j.molliq.2023.121797.

35. Z. Wen *et al*., Effect of Gemini surfactant structure on water/oil interfacial properties: A dissipative particle dynamics study, *Chem. Eng. Sci*. **251** (2022) 117466. https://doi.org/10.1016/j.ces.2022.117466.

36. M. D. Tomasini and M. Silvina Tomassone, Dissipative particle dynamics simulation of poly(ethylene oxide)-poly(ethyl ethylene) block copolymer properties for enhancement of cell membrane rupture under stress, *Chem. Eng. Sci*. **71** (2012) 400. https://doi.org/10.1016/j.ces.2011.10.061.

37. Y. L. Yang, Y. J. Sheng and H. K. Tsao, Hybridization of lipids to monolayer and bilayer membranes of triblock copolymers, *J. Colloid. Interface. Sci.* **544** (2019) 53. https://doi.org/10.1016/j.jcis.2019.02.071.

38. S. W. Hu, C. Y. Huang, H. K. Tsao and Y. J. Sheng, Hybrid membranes of lipids and diblock copolymers: From homogeneity to rafts to phase separation, *Phys. Rev. E* **99** (2019) 1. https://doi.org/10.1103/PhysRevE.99.012403.

39. K. Hpone Myint *et al*., Encapsulation of nanoparticles during polymer micelle formation: A dissipative particle dynamics study, *J. Phys. Chem. B* **120** (2016) 11582. https://doi.org/10.1021/acs.jpcb.6b07324.

40. J. D. Hernández Velázquez, S. Mejía-Rosales, A. Gama Goicochea, Nanorheology of poly- and monodispersed polymer brushes under oscillatory flow as models of epithelial cancerous and healthy cell brushes, *Polymer (Guildf)* **129** (2017) 44. https://doi.org/10.1016/j.polymer.2017.09.046.

41. E. Mayoral, A. Gama Goicochea, Modeling of Branched Thickening Polymers under Poiseuille Flow Gives Clues as to How to Increase a Solvent's Viscosity, *J. Phys. Chem. B* **125** (2021) 1692. https://doi.org/10.1021/acs.jpcb.0c11087.

42. E. I. Barcelos *et al*., Controlling particle penetration and depletion at the wall using Dissipative Particle Dynamics, *Comput. Phys. Commun*. **258** (2021) 107618. https://doi.org/10.1016/j.cpc.2020.107618.

43. J. D. Hernández Velázquez, G. Sánchez-Balderas, A. Gama Goicochea and E. Pérez, The effective interfacial tensions between pure liquids and rough solids: a coarse-grained simulation study, *Phys. Chem. Chem. Phys.* **25** (2023) 10325. https://doi.org/10.1039/D2CP04321A.

44. A. Gama Goicochea and Z. Nussinov, Topological phase transition in a quasi-two-dimensional Coulomb gas, *Phys. Rev. E* **107** (2023) 014104. https://doi.org/10.1103/PhysRevE.107.014104.

45. A. Gama Goicochea and E. Pérez, Scaling Law of the Disjoining Pressure Reveals 2D Structure of Polymeric Fluids, *Macromol. Chem. Phys.* **216** (2015) 1076. https://doi.org/10.1002/macp.201400623.

46. A. Gama Goicochea, Adsorption and disjoining pressure isotherms of confined polymers using dissipative particle dynamics, *Langmuir* **23** (2007) 11656. https://doi.org/10.1021/la701791h.

47. A. Gama Goicochea and F. Alarcón, Solvation force induced by short range, exact dissipative particle dynamics effective surfaces on a simple fluid and on polymer brushes, *J. Chem. Phys.* **134** (2011) 014703. https://doi.org/10.1063/1.3517869.

48. J.N. Israelachvili, Intermolecular and Surface Forces, 3rd ed. (Elsevier academic press, 2011).

49. K. A. Terrón-Mejia, R. López-Rendón and A. Gama Goicochea, Electrostatics in dissipative particle dynamics using Ewald sums with point charges, *J. Phys. Condens. Mat.* **28** (2016) 425101. https://doi.org/10.1088/0953-8984/28/42/425101.

50. M. Carrillo-Tripp, H. Saint-Martin and I. Ortega-Blake, A comparative study of the hydration of Na+ and K+ with refined polarizable model potentials, J. Chem. Phys. **118** (2003) 7062. https://doi.org/10.1063/1.1559673; R.D. Groot, Electrostatic interactions in dissipative particle dynamics-simulation of polyelectrolytes and anionic surfactants, *J. Chem. Phys.* **118** (2003) 11265. https://doi.org/10.1063/1.1574800; M. González-Melchor, E. Mayoral, M. E. Velázquez and J. Alejandre, Electrostatic interactions in dissipative particle dynamics using the Ewald sums, J. Chem. Phys. **125** (2006) 224107. https://doi.org/10.1063/1.2400223.

51. C. Ibergay, P. Malfreyt and D. J. Tildesley, Electrostatic interactions in dissipative particle dynamics: Toward a mesoscale modeling of the polyelectrolyte brushes, *J. Chem. Theory. Comput.* **5** (2009) 3245. https://doi.org/10.1021/ct900296s.

52. I.-C. Yeh and M. L. Berkowitz, Ewald summation for systems with slab geometry, *J. Chem. Phys.* **111** (1999) 3155. https://doi.org/10.1063/1.479595.

53. F. Alarcón, E. Pérez and A. Gama Goicochea, Dissipative particle dynamics simulations of weak polyelectrolyte adsorption on charged and neutral surfaces as a function of the degree of ionization, *Soft Matter* **9** (2013) 3777. https://doi.org/10.1039/c2sm27332b.

54. C. Pastorino and A. Gama Goicochea, Dissipative Particle Dynamics: A Method to Simulate Soft Matter Systems in Equilibrium and Under Flow, in: Environmental Science and Engineering, Springer Berlin Heidelberg, 2015: pp. 51-79. https://doi.org/10.1007/978-3-319-11487-3_3.

55. E. Mayoral, J. D. Hernández Velázquez and A. Gama Goicochea, The viscosity of polyelectrolyte solutions and its dependence on their persistence length, concentration and solvent quality, *RSC Adv.* **12** (2022) 35494. https://doi.org/10.1039/d2ra06990c.

56. I. Vattulainen, M. Karttunen, G. Besold and J. M. Polson, Integration schemes for dissipative particle dynamics simulations: From softly interacting systems towards hybrid models, *J. Chem. Phys.* **116** (2002) 3967. https://doi.org/10.1063/1.1450554.

57. M. E. Velázquez, A. Gama Goicochea, M. González-Melchor, M. Neria, J. Alejandre, Finite-size effects in dissipative particle dynamics simulations, *J. Chem. Phys.* **124** (2006) 084104. https://doi.org/10.1063/1.2166377.

58. A. O. Stone, M. J. Lea, P. Fozooni and J. Frost, The melting temperature of a two-dimensional electron solid on helium in a magnetic field, *J. Phys. Condens. Mat.* **2** (1990) 485. https://doi.org/10.1088/0953-8984/2/2/023.

59. Z. Hu *et al.*, Evidence of the Berezinskii-Kosterlitz-Thouless phase in a frustrated magnet, *Nat. Commun.* **11** (2020) 5631. https://doi.org/10.1038/s41467-020-19380-x.

60. N. Goldenfeld, Lectures on Phase Transitions and the Renormalization Group (CRC Press, 2018). https://doi.org/10.1201/9780429493492.

61. A. O. Parry and R. Evans, Finite-size-scaling derivation of the Widom critical-exponent relation for surface tension, *Phys. Rev. A (Coll Park)* **46** (1992) 5282. https://doi.org/10.1103/PhysRevA.46.5282.

62. E. Mayoral and A. Gama Goicochea, Hyperscaling relationship between the interfacial tension of liquids and their correlation length near the critical point, *Soft Matter* **10** (2014) 9054. https://doi.org/10.1039/c4sm01981d.

63. J. H. Irving and J. G. Kirkwood, The statistical mechanical theory of transport processes. IV. The equations of hydrodynamics, *J. Chem. Phys.* **18** (1950) 817. https://doi.org/10.1063/1.1747782.

64. A. Gama Goicochea, M. A. Balderas Altamirano, J. D. Hernández Velázquez and E. Pérez, The role of the dissipative and random forces in the calculation of the pressure of simple fluids with dissipative particle dynamics, *Comput. Phys. Commun.* **188** (2015) 76. https://doi.org/10.1016/j.cpc.2014.11.006.

65. M. R. Moldover, Interfacial tension of fluids near critical points and two-scale-factor universality, *Phys. Rev. A (Coll Park)* **31** (1985) 1022. https://doi.org/10.1103/PhysRevA.31.1022.

66. S. Klessinger and G. Münster, Numerical investigation of the interface tension in the three-dimensional Ising model, *Nucl. Phys. B* **386** (1992) 701. https://doi.org/10.1016/0550-3213(92)90634-N.

67. J. A. C. Valdez *et al.*, Influence of the temperature on the interfacial tension between organic solvent-hydrocarbon systems using Dissipative Particle Dynamics, *Fluid Phase Equilib.* **575** (2023) 113933. https://doi.org/10.1016/j.fluid.2023.113933.

68. K. Binder, Monte Carlo calculation of the surface tension for two- and three-dimensional lattice-gas models, *Phys. Rev. A (Coll Park)* **25** (1982) 1699. https://doi.org/10.1103/PhysRevA.25.1699.

69. A. M. Ferrenberg and D. P. Landau, Critical behavior of the three-dimensional Ising model: A high-resolution Monte Carlo study, *Phys. Rev. B* **44** (1991) 5081. https://doi.org/10.1103/PhysRevB.44.5081.

70. A. M. Ferrenberg, J. Xu and D. P. Landau, Pushing the limits of Monte Carlo simulations for the three-dimensional Ising model, *Phys. Rev. E* **97** (2018) 043301. https://doi.org/10.1103/PhysRevE.97.043301.

71. A. R. Honerkamp-Smith *et al*., Line Tensions, Correlation Lengths, and Critical Exponents in Lipid Membranes Near Critical Points, *Biophys. J.* **95** (2008) 236. https://doi.org/10.1529/biophysj.107.128421.

72. A. R. Honerkamp-Smith, S. L. Veatch and S. L. Keller, An introduction to critical points for biophysicists; observations of compositional heterogeneity in lipid membranes, *BBA-Biomembranes* **1788** (2009) 53. https://doi.org/10.1016/j.bbamem.2008.09.010.

73. J. M. Pusterla, S. A. Cannas, E. Schneck and R. G. Oliveira, Purified myelin lipids display a critical mixing point at low surface pressure, *BBA-Biomembranes* **1864** (2022) 183874. https://doi.org/10.1016/j.bbamem.2022.183874.

74. J. Clerouin, J.-P. Hansen and B. Piller, Two-dimensional classical electron gas in a periodic field: Delocalization and dielectric-plasma transition, *Phys. Rev. A (Coll Park)* **36** (1987) 2793. https://doi.org/10.1103/PhysRevA.36.2793.

75. B. Savoie, A rigorous proof of the Bohr-van Leeuwen theorem in the semiclassical limit, *Rev. Math. Phys.* **27** (2015) 1550019. https://doi.org/10.1142/S0129055X15500191.

76. G. S. Dubey and G. Gumbs, Melting and dynamics of two-dimensional Coulomb systems in the presence of a magnetic field, *Phys. Rev. B* **56** (1997) 2957. https://doi.org/10.1103/PhysRevB.56.2957.

77. G. Gumbs and G.S. Dubey, Effect of modulation and magnetic field on the properties of two-dimensional Coulomb systems, *Phys. Rev. B* **57** (1998) 3769. https://doi.org/10.1103/PhysRevB.57.3769.

78. K. R. Vidal and S. D. Baalrud, Extended space and time correlations in strongly magnetized plasmas, *Phys. Plasmas* **28** (2021) 042103. https://doi.org/10.1063/5.0045078.

79. P. Hartmann *et al*., Self-diffusion in two-dimensional quasi-magnetized rotating dusty plasmas, *Phys. Rev. E* **99** (2019) 013203. https://doi.org/10.1103/PhysRevE.99.013203.

80. D. Frenkel and B. Smit, Understanding Molecular Simulation, 2nd ed. (Academic Press, London, 2002).

81. D. Bohm, E. H. S. Burhop and H. S. W. Massey, The Use of Probes for Plasma Exploration in Strong Magnetic Fields, in: A. Guthrie, R.K. Wakerling (Eds.), The Characteristics of Electrical Discharges in Magnetic Fields, 1st ed., McGraw-Hill Book Company Inc., New York, 1949: pp. 13-66.

82. J. Daligault, Practical model for the self-diffusion coefficient in Yukawa one-component plasmas, *Phys. Rev. E* **86** (2012) 047401. https://doi.org/10.1103/PhysRevE.86.047401.

83. T. Ott, H. Löwen and M. Bonitz, Dynamics of two-dimensional one-component and binary Yukawa systems in a magnetic field, *Phys. Rev. E* **89** (2014) 013105. https://doi.org/10.1103/PhysRevE.89.013105.

84. S. D. Baalrud and J. Daligault, Transport regimes spanning magnetization-coupling phase space, *Phys. Rev. E* **96** (2017) 043202. https://doi.org/10.1103/PhysRevE.96.043202.

85. P. G. de Gennes, Scaling Concepts in Polymer Physics, 1st ed. (Cornell university press, 1979).

86. P. J. Flory, Principles of Polymer Chemistry, 1st ed. (Cornell university press, Ithaca, New York, 1953).

87. J. C. Le Guillou and J. Zinn-Justin, Critical Exponents for the n-Vector Model in Three Dimensions from Field Theory, *Phys. Rev. Lett.* **39** (1977) 95. https://doi.org/10.1103/PhysRevLett.39.95.

88. J. des Cloizeaux, The Lagrangian theory of polymer solutions at intermediate concentrations, *J. Phys. France* **36** (1975) 281. https://doi.org/10.1051/jphys:01975003604028100.

89. M. O. Gallyamov *et al*., Individual bottle brush molecules in dense 2D layers restoring high degree of extension after collapse-decollapse cycle: Directly measured scaling exponent, *Eur. Phys. J. E* **29** (2009) 73. https://doi.org/10.1140/epje/i2009-10451-5.

90. X. Wang and V. J. Foltz, Chain conformation in two-dimensional dense state, *J. Chem. Phys.* **121** (2004) 8158. https://doi.org/10.1063/1.1801331.

91. H. Meyer *et al*., Static properties of polymer melts in two dimensions, *J. Chem. Phys.* **132** (2010) 184904. https://doi.org/10.1063/1.3429350

92. B. Duplantier, Exact critical exponents for two-dimensional dense polymers, *J. Phys. A Math. Gen.* **19** (1986) L1009. https://doi.org/10.1088/0305-4470/19/16/011

93. A. Cavallo, M. Müller and K. Binder, Unmixing of Polymer Blends Confined in Ultrathin Films: Crossover between Two-Dimensional and Three-Dimensional Behavior, *J. Phys. Chem. B* **109** (2005) 6544. https://doi.org/10.1021/jp0458506